Mechanism of Particle-Mediated Inhibition of Demetalation for Single-Atom Catalytic Sites in Acidic Electrochemical Environments

Xiao-Bin Gao,[1] Yu-Cheng Wang,[1,2*] Wei-Cheng Xu,[1] Huan Huang,[3] Kuang-Min Zhao,[1*] Hong Ye,[2] Zhi-You Zhou,[1,2] Nan-Feng Zheng[1,2*] and Shi-Gang Sun[1]

[1]State Key Laboratory of Physical Chemistry of Solid Surfaces, College of Chemistry and Chemical Engineering, Xiamen University, Xiamen 361005, China.

[2]Innovation Laboratory for Sciences and Technologies of Energy Materials of Fujian Province (IKKEM), Xiamen 361005, China.

[3]Beijing Synchrotron Radiation Facility, Institute of High Energy Physics, Chinese Academy of Sciences, Beijing, 100049, China.

†These authors contributed equally to this work.

*Corresponding author. Email: wangyc@xmu.edu.cn, kmzhao@xmu.edu.cn, nfzheng@xmu.edu.cn.

Abstract: Demetalation, caused by the electrochemical dissolution of metal atoms, poses a significant challenge to the practical application of single-atom catalytic sites (SACS) in proton exchange membrane-based energy technologies. One promising approach to inhibit SACS demetalation is the use of metallic particles to interact with SACS. However, the mechanism underlying this stabilization remains unclear. In this study, we propose and validate a unified mechanism by which metal particles can inhibit the demetalation of Fe SACS. Metal particles act as electron donors, decreasing the Fe valence by increasing the electron density at the FeN_4 position, thereby strengthening the Fe-N bond, and inhibiting electrochemical Fe dissolution. Different types, forms, and contents of metal particles increase the Fe-N bond strength to varying extents. A linear correlation between Fe valence, Fe-N bond strength, and electrochemical Fe dissolution amount supports this mechanism. Our screening of a particle-assisted Fe SAC led to a 78% reduction in Fe dissolution, enabling continuous operation for up to 430 hours in a fuel cell. These findings contribute to the development of stable SACS for energy applications.

Single-atom catalytic sites (SACS) have become an emerging frontier in catalysis and material science[1-3]. Carbon-based non-precious metal SACS, such as Fe, have shown great promise in catalyzing several key electrochemical reactions such as the oxygen reduction reaction (ORR) and oxygen evolution reaction (OER)[4-6]. Thanks to the mature technology of proton exchange membrane (PEM) electrolysis or fuel cells, SACS in acidic electrochemical environments are of particular interest[7-9]. While numerous studies have focused on the activity and selectivity of Fe SACS in acidic electrocatalysis, limited attention has been given to their degradation through electrochemical dissolution, which can lead to the demetalation of Fe SACS[5, 10-11]. This is a serious issue because demetalation destroys active sites, contaminates polymer electrolytes, and generates corrosive radicals, all of which can negatively impact the performance of the SACS[12-14]. Previous studies have theoretically and experimentally demonstrated that Fe SACS are susceptible to dissolving in acidic electrochemical environments[15-16]. Therefore, addressing the issue of demetalation should be a top priority before Fe SACS can move into practical application.

Efficient strategies for preventing the demetalation of SACS have been reported sparingly. Recent studies have shown that interaction with metallic particles can inhibit the demetalation of SACs, making it one of the few strategies that offer promise for inhibiting demetalation[17]. However, the mechanisms that underlie the stabilization of SACs by metallic particles remain poorly understood. The specific property or properties of SACS that are altered following the introduction of particles and how such modifications prevent demetalation are yet to be fully elucidated. One major challenge lies in the difficulty of distinguishing changes in SACs due to overlapping signals when using particles with the same elemental composition. This also makes it challenging to quantify accurately the number of SACs undergoing electrochemical dissolution. Furthermore, it is unclear whether the stabilization mechanism varies with different types of metallic particles, their physical forms, or their content[17-19]. Addressing these questions is critical to advancing our knowledge of the interaction between SACs and metallic particles and developing effective strategies for inhibiting demetalation.

In this study, we fabricated a Fe SACS-particle catalyst system where the particle consisted of Pt or Au instead of Fe. This design allowed for precise determination of the property changes and dissolution amount of Fe SACS. By employing online electrochemical inductively coupled plasma mass spectrometry (ICP-MS), advanced X-ray absorption spectroscopy (XAS), and theoretical calculations, we were able to establish a linear correlation between Fe valence, Fe-N bond strength, and electrochemical Fe dissolution amount. Subsequently, we proposed a unified mechanism in which metallic particles act as electron donors, leading to a decrease in Fe valence by increasing electron density of the carbon plane, particularly at the FeN_4 position. This strengthens Fe-N coordination and inhibits electrochemical Fe dissolution. Different types (such as Pt, Pd, Au, Ag, Fe, Co, and Ni), physical forms (such as size, location, and crystallinity), and contents of metal particles increase the Fe-N bond strength to varying extents. Lastly, we screened a particle-assisted Fe SAC with an impressive 78% decline in Fe dissolution, which ran stably for up to 430 hours in

fuel cells.

Results

The Fe single-atom catalyst (Fe_{sac}) was prepared through a two-step pyrolysis coupled with an acid-leaching method, as described in previous studies[20-21]. X-ray diffraction (XRD) and transition electron microscopy (TEM) analyses indicated the absence of nanoparticles in Fe_{sac}, as shown in Figures S1 and S2, respectively. Fourier-transformed k^3-weighted extended X-ray absorption fine structure (EXAFS) revealed a prominent Fe-N peak at 1.46 Å and a minor Fe-Fe peak at 2.1 Å (Figures S3), corroborating that Fe was primarily in an atomically dispersed form[22-23]. Pt-Fe_{sac} and Au-Fe_{sac} were synthesized through the impregnation reduction method, with similar metallic content (Table S1) and average particle size (Figure S4). The three catalysts' Fe valence, including Fe_{sac}, was measured by X-ray absorption near-edge structure (XANES), and followed the order of Pt-Fe_{sac} < Au-Fe_{sac} < Fe_{sac}, as shown in Figure S5. The atomically dispersed Fe sites were maintained in all three catalysts, as shown in Figure S6.

Electrochemical Fe dissolution was monitored through online ICP-MS. As depicted in Figures 1a-c, all catalysts exhibited potential-dependent Fe dissolution behavior, with an onset potential of approximately 0.8 V versus the reversible hydrogen electrode (RHE). However, the amount of Fe dissolution varied significantly among the catalysts, as shown quantitatively in Figure 1d. The Fe dissolution amount followed the order of Pt-Fe_{sac} < Au-Fe_{sac} < Fe_{sac}, consistent with the trend of decreasing Fe valence. This consistency suggested that metallic particles decreased the Fe valence and inhibited electrochemical Fe dissolution. Additionally, the Pt case showed a lower Fe valence and correspondingly lower Fe dissolution amount compared to the Au case.

Theoretical calculations were then conducted to gain insight into the demetalization behavior upon the addition of metallic particles and to elucidate the observed correlation between Fe valence and Fe dissolution. For this purpose, a graphene plane hosting the FeN_4 site was used as the structural model of the Fe SACS, as depicted in Figure 2a. Subsequently, a Pt_{19} cluster was placed above the graphene plane, in close proximity to the FeN_4 position, as shown in Figure 2b. The transfer of electrons from the cluster to the carbon plane, which enriches the FeN_4 position, was revealed by the charge density difference map in Figure 2c. As demetalation of the FeN_4 site involves the breakage of Fe-N bonds, the strength of the Fe-N bond was employed as a descriptor of demetalation[16]. Specifically, the negative of the projected crystal orbital Hamilton population (-pCOHP) was utilized to quantitatively compare the Fe-N bond strength. As illustrated in Figures 2d and 2e, the integrated negative of the projected crystal orbital Hamilton population (-ICOHP) increased from 2.517 to 2.644 following Pt loading, indicating a stronger Fe-N bond[24-25]. This result suggests that the Pt particle increases the electron density at the FeN_4 position, preferentially enhancing the bonding component and consequently strengthening the Fe-N bond[26]. Theoretical calculations also revealed that the distance between the particle and SACS significantly affects the Fe valence and Fe-N bond strength, as demonstrated in Figure S7.

To expand the generalizability of the conclusion, six additional metals (Pd, Au, Ag, Fe, Co, and Ni) were chosen, in which the distance between the particle and the single-atom site was kept constant. The analysis of –pCOHP is shown in Figure S8, and the Barder valence electron number (N) is summarized in Table S2. A positive linear correlation between –COHP and N was established, as demonstrated in Figure 2f. The larger N value suggested a higher electron density at the Fe center, corresponding to a lower Fe valence[26-27]. The higher –ICOHP indicated a stronger Fe-N bond, which led to a decrease in demetallation[24-25]. This positive correlation strongly supported the idea that

metallic particles could act as electron donors, increasing the electron density at the FeN_4 position and strengthening the Fe-N bond, thus inhibiting electrochemical Fe dissolution. Furthermore, the observed strengthening of the Fe-N bond varied depending on the type of metal used. These findings are consistent with the experimental outcomes and lend support to the proposed mechanism.

To further investigate the influence of the physical characteristics of particles, such as size, location, and crystallinity, as well as the metal content on Fe valence and dissolution, Pt particles were used as an example. In this study, five Pt-loaded Fe_{sac} catalysts were synthesized using different reducing agents, loading protocols, and cleaning temperatures. The five catalysts were labeled Pt-Fe_{sac}-EG_1–350, Pt-Fe_{sac}-EG_1–RT, Pt-Fe_{sac}-EG_2–350, Pt-Fe_{sac}-EG_2–RT, and Pt-Fe_{sac}-BA_2–350, based on the synthetic conditions employed. Here, the terms EG and BA refer to ethylene glycol and benzoic acid reducing agents, respectively. The numbers 1 and 2 represent Pt(IV) reduction that occurred simultaneously with particle loading and prior to particle loading, respectively. Furthermore, 350 and RT refer to the catalyst cleaning temperatures that were set at 350 °C and room temperature, respectively.

As summarized in Table S3, the Pt-loaded Fe_{sac} exhibited varying Pt content ranging from 0.576 to 1.15 wt.%. The average particle size of these samples, determined through statistical analysis with TEM, ranged from 1 to 15 nm, as indicated in Figure S9. The crystallinity of the Pt particles across the samples also varied, with some showing an amorphous structure while others exhibited a face-centered cubic phase. These differences were analyzed with XRD and presented in Figure S10. Since Fe sites were uniformly dispersed on the carbons, the average distance between the particles and the single atoms was influenced by the varying Pt contents and particle sizes. The Fe valence of the six catalysts was compared using XANES and followed the order: Pt-Fe_{sac}-EG_1–RT < Pt-Fe_{sac}-EG_1–350 < Pt-Fe_{sac}-EG_2–RT < Pt-Fe_{sac}-BA_2–350 < Pt-Fe_{sac}-EG_2–350 < Fe_{sac}, as demonstrated in Figure 3a. The addition of Pt particles led to a decrease in the Fe valence to different extents, but did not alter the atomically dispersed state of the Fe sites, as shown in Figure S11. To determine if the observed changes in Fe valence were solely due to the treatment during the synthetic process, a control sample (Fe_{sac}-EG_1–350) was prepared using the same synthetic protocol as Pt-Fe_{sac}-EG_1–350 without adding any Pt salt. The two samples exhibited nearly identical Fe valence, thus verifying that the particles were responsible for the observed changes in Fe valence, as presented in Figure S12.

The electrochemical Fe dissolution of the Pt-loaded Fe_{sac} was compared, as depicted in Figure 3b. Quantitative analysis of Fe dissolution revealed significant differences across the samples, as presented in Figure 3c. Interestingly, a positive linear correlation was observed between the Fe valence and dissolution amount, as demonstrated in Figure 3d. Notably, the Au-Fe_{sac} sample also adhered to this linear correlation, supporting the notion that different types, forms, and contents of metal particles can affect the Fe valence and thereby modify the degree of Fe-N bond strengthening.

The Pt-Fe_{sac}-EG_1–350 sample, exhibiting the lowest Fe dissolution amount with a 78% decrease in Fe dissolution, was chosen for performance testing using a PEM-based fuel cell. The Pt state of the catalyst was meticulously characterized. XANES analysis, presented in Figure S13, revealed that the average Pt valence in the Pt-Fe_{sac}-EG_1–350 catalyst was higher than that in the Pt foil reference. This higher valence was attributed to the partial surface oxidation of Pt particles[28] and corroborated by X-ray photoelectron spectroscopy (XPS) analysis depicted in Figure S14. Furthermore, the deposition of Pt particles had a minimal effect on the pore structure of the pristine Fe_{sac}, as demonstrated in Figure S15.

Interestingly, the Pt particles were found to be inactive in the ORR process in this catalyst. During the RDE test, both the bare Fe_{sac} sample and the Pt-Fe_{sac}-EG_1–350 exhibited nearly identical half-waves of 0.804 V (blue line in Figure 4a) and 0.798 V (red line in Figure 4b), respectively, versus RHE. This observation suggested that the Pt particles did not contribute to the ORR activity. To further validate this conclusion, a methanol poisoning experiment was conducted, which revealed that Fe_{sac} and Pt-Fe_{sac}-EG_1–350 exhibited negligible activity loss even after adding 0.2 M methanol into the electrolyte, indicating the high tolerance of the FeN_4 site towards methanol in acidic media[29-30]. This confirmed that the Pt particles were indeed inactive in the ORR process; otherwise, an apparent methanol electro-oxidation signal would have been observed[31], as evidenced by the Pt/C case (orange line in Figure 4c). The undetectable ORR activity of Pt particles could be attributed to their surface oxide coverage, leading to the loss of the hydrogen adsorption/desorption region[32], as demonstrated in Figure S16. Additionally, the low Pt loading and small particle size may also contribute to the lack of detectable ORR activity. It may be concerning whether the inactive Pt particles could be activated during the durability test process. To address this concern, a methanol poisoning experiment was conducted after the accelerated decay test, as presented in Figure S17, which revealed no methanol response signal. This supported the conclusion that the Pt particles were indeed ORR-inert throughout the entire test.

Finally, Pt-Fe_{sac}-EG_1–350 was utilized as a cathode catalyst in a direct methanol fuel cell (DMFC) with oxygen as the oxidant. The Pt-Fe_{sac}-EG_1–350 cathode exhibited a current density of 230 mA cm^{-2} at 0.4 V and a peak power density (P_{max}) of 146 mW cm^{-2}, which was slightly higher than that of Fe_{sac} (180 mA cm^{-2} @ 0.4 V and P_{max} = 140 mW cm^{-2}), as shown in Figure 4d. Notably, this was the highest reported P_{max} in DMFC to date with non-precious metal materials as the cathode catalyst, as evidenced in Figure 4f and Table S4. In addition to activity, fuel cell operation stability is crucial. As depicted in Figure 4e, the cell voltage rapidly decreased from 0.49 to 0.40 V within the first 10 hours and then remained stable at this level for up to 430 hours of the stability test. These data positioned Pt-Fe_{sac}-EG_1–350 as the most stable catalyst among all previously reported M-N-C materials in DMFC, as reflected in Figure 4g and Table S4. In comparison, bare Fe_{sac} demonstrated a loss of 56% in cell voltage within the first 100 hours of fuel cell operation. The morphology and structure of the Pt-Fe_{sac}-EG_1–350 catalyst after 430 hours of fuel cell testing were analyzed using high-angle annular dark-field scanning transmission electron microscopy (HAADF-STEM). No obvious particle agglomeration was observed after the stability test in Figure S18; however, the average particle size decreased from 1.5 to 1.2 nm, and the lattice structure was significantly destroyed (Figure S19). This change may have resulted from the dissolution of Pt during the electrochemical process, as supported by the online ICP-MS experiment (Figure S20) and lessened the effect of Pt particles on the Fe SACS. Although the reduced Fe dissolution may not be the sole reason for the improved stability during the fuel cell test, it should be considered a crucial factor.

To summarize, this study quantitatively described the interaction between a single Fe site and metallic particles and its impact on demetallation. Metallic particles acted as electron donors, increasing the electron density at the FeN_4 site, strengthening the Fe-N coordination bond, inhibiting the electrochemical dissolution of Fe, and enhancing catalyst stability. This mechanism is consistent across different types, forms, and contents of metal particles As a result, a stable particle-assisted Fe-based ORR catalyst was identified that can operate stably for up to 430 hours in DMFC. This study is significant for developing stable SACS for fuel cells and other applications beyond.

References

1. Qiao, B.; Wang, A.; Yang, X.; Allard, L. F.; Jiang, Z.; Cui, Y.; Liu, J.; Li, J.; Zhang, T., Single-atom catalysis of CO oxidation using Pt_1/FeO_x. *Nat. Chem.* **2011,** *3* (8), 634-41.

2. Zhu, C.; Fu, S.; Shi, Q.; Du, D.; Lin, Y., Single-Atom Electrocatalysts. *Angew.Chem. Int.Ed.* **2017,** *56* (45), 13944-13960.

3. Liang, X.; Fu, N.; Yao, S.; Li, Z.; Li, Y., The Progress and Outlook of Metal Single-Atom-Site Catalysis. *J. Am. Chem. Soc.* **2022,** *144* (40), 18155-18174.

4. Zhang, H.; Chung, H. T.; Cullen, D. A.; Wagner, S.; Kramm, U. I.; More, K. L.; Zelenay, P.; Wu, G., High-performance fuel cell cathodes exclusively containing atomically dispersed iron active sites. *Energy Environ. Sci.* **2019,** *12* (8), 2548-2558.

5. Mehmood, A.; Gong, M.; Jaouen, F.; Roy, A.; Zitolo, A.; Khan, A.; Sougrati, M.-T.; Primbs, M.; Bonastre, A. M.; Fongalland, D.; Drazic, G.; Strasser, P.; Kucernak, A., High loading of single atomic iron sites in Fe–NC oxygen reduction catalysts for proton exchange membrane fuel cells. *Nat. Catal.* **2022,** *5* (4), 311-323.

6. Wang, X.; Sun, L.; Zhou, W.; Yang, L.; Ren, G.; Wu, H.; Deng, W.-Q., Iron single-atom catalysts confined in covalent organic frameworks for efficient oxygen evolution reaction. *Cell Reports Physical Science* **2022,** *3* (3).

7. King, L. A.; Hubert, M. A.; Capuano, C.; Manco, J.; Danilovic, N.; Valle, E.; Hellstern, T. R.; Ayers, K.; Jaramillo, T. F., A non-precious metal hydrogen catalyst in a commercial polymer electrolyte membrane electrolyser. *Nat. Nanotechnol.* **2019,** *14* (11), 1071-1074.

8. Liu, S.; Li, C.; Zachman, M. J.; Zeng, Y.; Yu, H.; Li, B.; Wang, M.; Braaten, J.; Liu, J.; Meyer, H. M.; Lucero, M.; Kropf, A. J.; Alp, E. E.; Gong, Q.; Shi, Q.; Feng, Z.; Xu, H.; Wang, G.; Myers, D. J.; Xie, J.; Cullen, D. A.; Litster, S.; Wu, G., Atomically dispersed iron sites with a nitrogen–carbon coating as highly active and durable oxygen reduction catalysts for fuel cells. *Nat. Energy* **2022,** *7* (7), 652-663.

9. Wu, Z. Y.; Chen, F. Y.; Li, B.; Yu, S. W.; Finfrock, Y. Z.; Meira, D. M.; Yan, Q. Q.; Zhu, P.; Chen, M. X.; Song, T. W.; Yin, Z.; Liang, H. W.; Zhang, S.; Wang, G.; Wang, H., Non-iridium-based electrocatalyst for durable acidic oxygen evolution reaction in proton exchange membrane water electrolysis. *Nat. Mater.* **2023,** *22* (1), 100-108.

10. Jiao, L.; Li, J.; Richard, L. L.; Sun, Q.; Stracensky, T.; Liu, E.; Sougrati, M. T.; Zhao, Z.; Yang, F.; Zhong, S.; Xu, H.; Mukerjee, S.; Huang, Y.; Cullen, D. A.; Park, J. H.; Ferrandon, M.; Myers, D. J.; Jaouen, F.; Jia, Q., Chemical vapour deposition of Fe-N-C oxygen reduction catalysts with full utilization of dense Fe-N(4) sites. *Nat. Mater.* **2021,** *20* (10), 1385-1391.

11. Liu, K.; Fu, J.; Lin, Y.; Luo, T.; Ni, G.; Li, H.; Lin, Z.; Liu, M., Insights into the activity of single-atom Fe-N-C catalysts for oxygen reduction reaction. *Nat. Commun.* **2022,** *13* (1), 2075.

12. Chenitz, R.; Kramm, U. I.; Lefèvre, M.; Glibin, V.; Zhang, G.; Sun, S.; Dodelet, J.-P., A specific demetalation of $Fe–N_4$ catalytic sites in the micropores of NC_Ar + NH_3 is at the origin of the initial activity loss of the highly active Fe/N/C catalyst used for the reduction of oxygen in PEM fuel cells. *Energy Environ. Sci.* **2018,** *11* (2), 365-382.

13. Shao, Y.; Dodelet, J. P.; Wu, G.; Zelenay, P., PGM-Free Cathode Catalysts for PEM Fuel Cells: A Mini-Review on Stability Challenges. *Adv. Mater.* **2019,** *31* (31).

14. Wan, X.; Liu, X.; Shui, J., Stability of PGM-free fuel cell catalysts: Degradation mechanisms and mitigation strategies. *Prog. Nat. Sci.* **2020,** *30* (6), 721-731.

15. Choi, C. H.; Baldizzone, C.; Grote, J. P.; Schuppert, A. K.; Jaouen, F.; Mayrhofer, K. J., Stability of Fe-N-C Catalysts in Acidic Medium Studied by Operando Spectroscopy. *Angew.Chem. Int.Ed.* **2015,** *54* (43), 12753-7.

16. Holby, E. F.; Wang, G.; Zelenay, P., Acid Stability and Demetalation of PGM-Free ORR Electrocatalyst Structures from Density Functional Theory: A Model for "Single-Atom Catalyst" Dissolution. *ACS Catal.* **2020,** *10* (24), 14527-14539.

17. Wan, X.; Liu, Q.; Liu, J.; Liu, S.; Liu, X.; Zheng, L.; Shang, J.; Yu, R.; Shui, J., Iron atom-cluster interactions increase activity and improve durability in Fe-N-C fuel cells. *Nat. Commun.* **2022,** *13* (1), 2963.

18. Wei, X.; Song, S.; Cai, W.; Luo, X.; Jiao, L.; Fang, Q.; Wang, X.; Wu, N.; Luo, Z.; Wang, H.; Zhu, Z.; Li, J.; Zheng, L.; Gu, W.; Song, W.; Guo, S.; Zhu, C., Tuning the spin state of Fe single atoms by Pd nanoclusters enables robust oxygen reduction with dissociative pathway. *Chem* **2023,** *9* (1), 181-197.

19. Zheng, F.-Y.; Li, R.; Xi, S.; Ai, F.; Wang, J., Engineering an iron atom-cluster nanostructure towards efficient and durable electrocatalysis. *J. Mater. Chem. A* **2023,** *11* (15), 8202-8212.

20. Wang, Q.; Zhou, Z. Y.; Lai, Y. J.; You, Y.; Liu, J. G.; Wu, X. L.; Terefe, E.; Chen, C.; Song, L.; Rauf, M.; Tian, N.; Sun, S. G., Phenylenediamine-based FeN(x)/C catalyst with high activity for oxygen reduction in acid medium and its active-site probing. *J. Am. Chem. Soc.* **2014,** *136* (31), 10882-5.

21. Wang, Y. C.; Lai, Y. J.; Song, L.; Zhou, Z. Y.; Liu, J. G.; Wang, Q.; Yang, X. D.; Chen, C.; Shi, W.; Zheng, Y. P.; Rauf, M.; Sun, S. G., S-Doping of an Fe/N/C ORR Catalyst for Polymer Electrolyte Membrane Fuel Cells with High Power Density. *Angew.Chem. Int.Ed.* **2015,** *54* (34), 9907-10.

22. Zitolo, A.; Goellner, V.; Armel, V.; Sougrati, M. T.; Mineva, T.; Stievano, L.; Fonda, E.; Jaouen, F., Identification of catalytic sites for oxygen reduction in iron- and nitrogen-doped graphene materials. *Nat. Mater.* **2015,** *14* (9), 937-42.

23. Marshall-Roth, T.; Libretto, N. J.; Wrobel, A. T.; Anderton, K. J.; Pegis, M. L.; Ricke, N. D.; Voorhis, T. V.; Miller, J. T.; Surendranath, Y., A pyridinic Fe-N(4) macrocycle models the active sites in Fe/N-doped carbon electrocatalysts. *Nat. Commun.* **2020,** *11* (1), 5283.

24. Niu, H.; Wang, X.; Shao, C.; Liu, Y.; Zhang, Z.; Guo, Y., Revealing the oxygen reduction reaction activity origin of single atoms supported on g-C_3N_4 monolayers: a first-principles study. *J. Mater. Chem. A* **2020,** *8* (14), 6555-6563.

25. Xiao, F.; Wang, Y.; Xu, G. L.; Yang, F.; Zhu, S.; Sun, C. J.; Cui, Y.; Xu, Z.; Zhao, Q.; Jang, J.; Qiu, X.; Liu, E.; Drisdell, W. S.; Wei, Z.; Gu, M.; Amine, K.; Shao, M., Fe-N-C Boosts the Stability of Supported Platinum Nanoparticles for Fuel Cells. *J. Am. Chem. Soc.* **2022,** *144* (44), 20372-20384.

26. Huang, H.; Yu, D.; Hu, F.; Huang, S. C.; Song, J.; Chen, H. Y.; Li, L. L.; Peng, S., Clusters Induced Electron Redistribution to Tune Oxygen Reduction Activity of Transition Metal Single-Atom for Metal-Air Batteries. *Angew.Chem. Int.Ed.* **2022,** *61* (12), e202116068.

27. Wan, X.; Shui, J., Exploring Durable Single-Atom Catalysts for Proton Exchange Membrane Fuel Cells. *ACS Energy Lett.* **2022,** *7* (5), 1696-1705.

28. Yoshida, H.; Nonoyama, S.; Yazawa, Y.; Hattori, T., Quantitative determination of platinum oxidation state by XANES analysis. *Phys Scripta* **2005,** *T115*, 813-815.

29. Sebastián, D.; Serov, A.; Matanovic, I.; Artyushkova, K.; Atanassov, P.; Aricò, A. S.; Baglio, V., Insights on the extraordinary tolerance to alcohols of Fe-N-C cathode catalysts in highly performing direct alcohol fuel cells. *Nano Energy* **2017,** *34*, 195-204.

30. Shi, Q.; He, Y.; Bai, X.; Wang, M.; Cullen, D. A.; Lucero, M.; Zhao, X.; More, K. L.; Zhou, H.; Feng, Z.; Liu, Y.; Wu, G., Methanol tolerance of atomically dispersed single metal site catalysts: mechanistic understanding and high-performance direct methanol fuel cells. *Energy Environ. Sci.* **2020,** *13* (10), 3544-3555.

31. Zhu, J.; Xia, L.; Yu, R.; Lu, R.; Li, J.; He, R.; Wu, Y.; Zhang, W.; Hong, X.; Chen, W.; Zhao, Y.; Zhou, L.; Mai, L.; Wang, Z., Ultrahigh Stable Methanol Oxidation Enabled by a High Hydroxyl Concentration on Pt Clusters/MXene Interfaces. *J. Am. Chem. Soc.* **2022,** *144* (34), 15529-15538.

32. Mechler, A. K.; Sahraie, N. R.; Armel, V.; Zitolo, A.; Sougrati, M. T.; Schwämmlein, J. N.; Jones, D. J.; Jaouen, F., Stabilization of Iron-Based Fuel Cell Catalysts by Non-Catalytic Platinum. *J. Electrochem. Soc.* **2018,** *165* (13), F1084-F1091.

Acknowledgments
We acknowledge the staff of the Beijing Synchrotron Radiation Facility (1W1B, BSRF) for their support in XAS measurements. **Funding:** This work was supported by National Natural Science Foundation of China (22021001, 22179116, 22288102), Fundamental Research Funds for the Central Universities (20720220017).

Author contributions: Y.-C. W. and N.-F. Z. designed the experiments. K.-M. Z. conducted the theoretical calculation. X.-B. G. performed most of the synthesis, characterization, and electrochemical tests. W.-C. X. and H. Y. conducted the on-line ICP-MS test. H. H. performed the XAS measurement. Z.-Y. Z. modified the manuscript. S.-G. S. supervised the research.

Competing interests: The authors declare no competing financial interests.

Data and materials availability: All results are reported in the main text and supplementary materials.

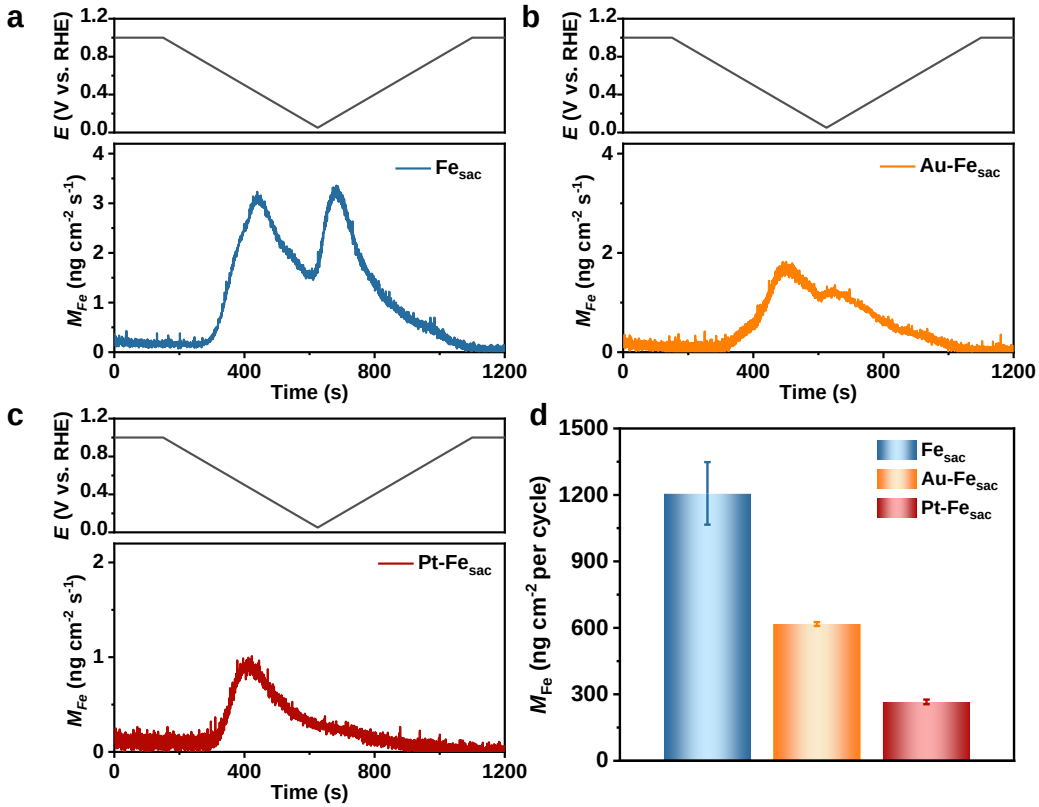

Figure 1. On line monitoring of electrochemical dissolution. (a-c) Real-time Fe dissolution rates for Fe_{sac}, Au-Fe_{sac} and Pt-Fe_{sac}. Test conditions: Ar-saturated 0.1 M $HClO_4$, with a scan rate of 2 mV s^{-1}, a catalyst loading of 0.48 mg cm^{-2}. **(d)** Quantitative comparison of the amount of Fe dissolution among the three catalysts during a single potential cycle.

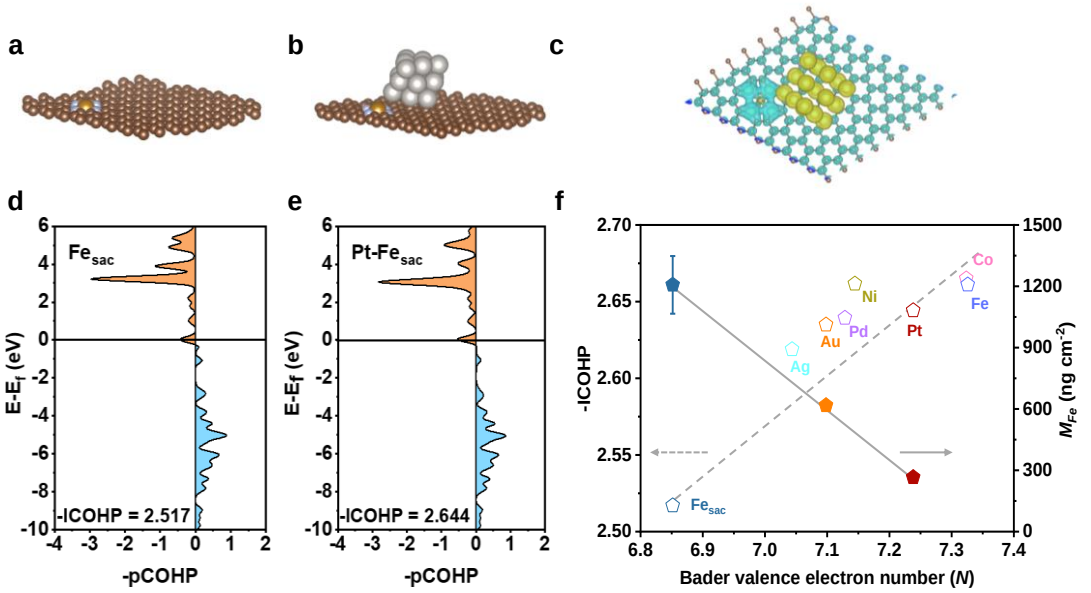

Figure 2. Theoretical calculations. (a, b) Optimized structural modes of Fe_{sac} and Pt-Fe_{sac}. (c) Charge density difference of Pt-Fe_{sac}. Yellow and cyan regions represent the accumulation of positive and negative charges, respectively. **(c)** Charge density difference of Pt-Fe_{sac}. Yellow and cyan regions represent the accumulation of positive and negative charges, respectively. **(d, e)** COHP analysis and the corresponding ICOHP values of the Fe-N bond in Fe_{sac} and Pt-Fe_{sac}, respectively. **(f)** Linear correlation between –ICOHP and Bader valence electron number (*N*) in various single atom-particle catalyst systems. Metallic particles used included Pt, Pd, Au, Ag, Fe, Co, and Ni. The amount of Fe dissolution for Fe_{sac}, Au-Fe_{sac} and Pt-Fe_{sac} was also shown, consistent with the theoretical calculation.

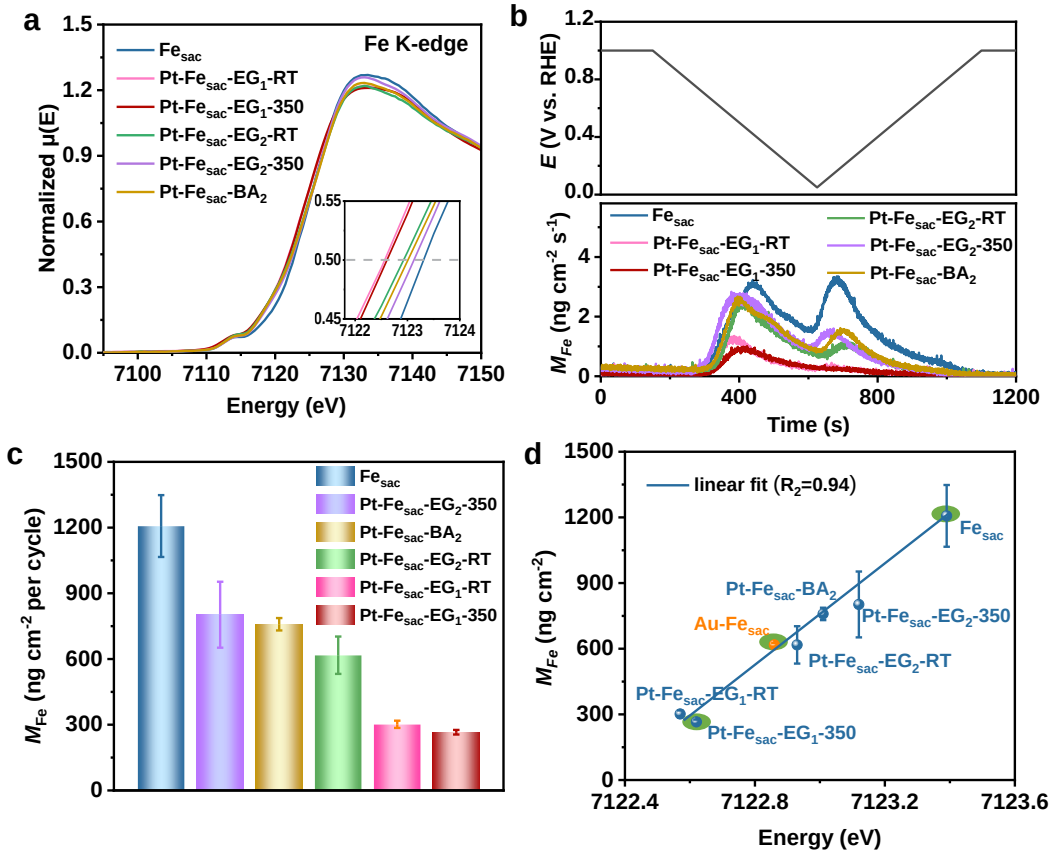

Figure 3. Linear correlation between Fe valence and the amount of Fe dissolution. (a) Fe K-edge XANES spectra of six catalysts. **(b)** Real-time Fe dissolution rate of six catalysts during a single potential cycle of 0.05~1.0 V. Test conditions: Ar-saturated 0.1 M $HClO_4$, 2 mV s^{-1} of scan rate, and 0.48 mg cm^{-2} of catalyst loading. **(c)** Quantitively comparison of Fe dissolution of the six catalysts amounts during a single potential cycle. **(d)** Linear correlation between the Fe valence and the amount of Fe dissolution, including all seven synthesized catalysts.

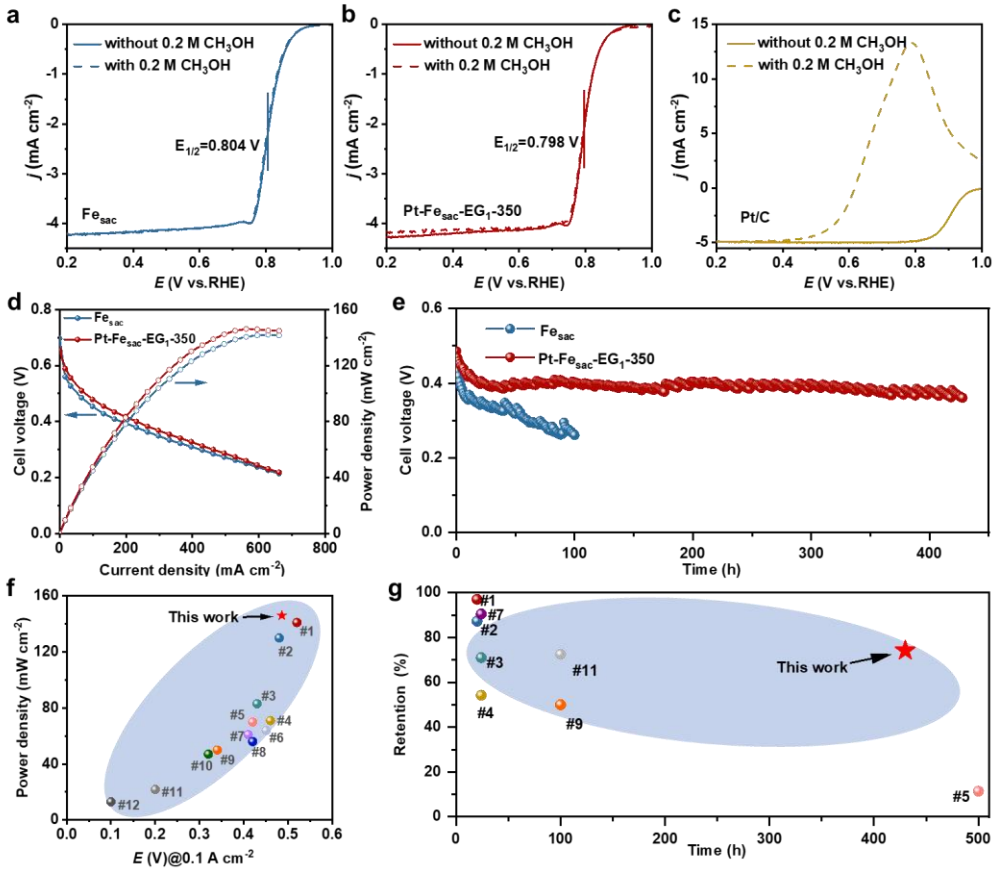

Figure 4. Fuel cell application. (a-c) Polarization curves of Fe_{sac}, Pt-Fe_{sac}-EG_1–350, and Pt/C in O_2-saturated 0.1 M $HClO_4$ solution with and without adding 0.2 M methanol. Test conditions: catalyst loading of 0.6 mg cm^{-2} for Fe_{sac} and Pt-Fe_{sac}-EG_1–350, loading of 0.18 mg cm^{-2} for 40 wt.% Pt/C catalyst, scan rate of 10 mV s^{-1}, and rotating rate of 900 rpm. **(d)** DMFC polarization and power density plots of Fe_{sac} (blue) and Pt-Fe_{sac}-EG_1–350 (red). **(e)** Long-term stability test at a constant current density of 0.1 A cm^{-2}. Test conditions: 80 °C cell temperature, 1 bar backpressure, 3 M CH_3OH fed to the anode, 0.2 SLPM of O_2 with 100% RH fed to the cathode, 1.21 cm^2 of geometric area, Nafion 212 Membrane, the Fe_{sac} or Pt-Fe_{sac}-EG_1–350 catalysts with a loading of 4.0 mg cm^{-2} at the cathode, and commercial $Pt_{40}Ru_{20}$/C catalyst with a loading of 4 mg cm^{-2} at the anode. **(f)** Comparison of P_{max} and cell voltage at 0.1 A cm^{-2} for all previously reported M-N-C catalysts in DMFC. **(g)** Comparison of the relative retention of catalyst activity after stability test for all previously reported M-N-C catalysts in DMFC.